



Origin of hetero-nuclear Au-Co dual atoms for efficient acidic oxygen reduction

Fanpeng Kong^{a,b,1}, Rutong Si^{c,1}, Ning Chen^e, Qi Wang^f, Junjie Li^b, Geping Yin^a, Meng Gu^f, Jiajun Wang^{a,*}, Li-Min Liu^{d,*}, Xueliang Sun^{b,*}

^a MIIT Key Laboratory of Critical Materials Technology for New Energy Conversion and Storage, Harbin Institute of Technology, 150001, China

^b Department of Mechanical and Materials Engineering, University of Western Ontario, London, ON N6A 5B9, Canada

^c Beijing Computational Science Research Center, Beijing 100083, China

^d School of Physics, Beihang University, Beijing 100083, China

^e Canadian Light Source Inc, Saskatoon, SK S7N 2V3, Canada

^f Department of Materials Science and Engineering, Southern University of Science and Technology, Shenzhen 518055, China

ARTICLE INFO

Keywords:

Hetero-nuclear dual atoms
Acid oxygen reduction
Fuel cells
Synergistic effect
D-orbitals symmetry

ABSTRACT

The atomically dispersed dual metal atom catalysts exhibit significant promise for the electrochemical energy conversion technologies. Herein, the hetero-nuclear precious-non-precious (Au-Co) dual atoms have been synthesized and subsequently applied for the acidic oxygen reduction reaction (ORR). The (Au-Co) dual atoms exhibit an outstanding activity with half-wave potential ($E_{1/2}$) of 0.82 V in 0.1 M HClO₄. Additionally, the proton exchange membrane fuel cell (PEMFC) analysis reveals a peak power density of 360 mW cm⁻² under H₂/air condition. Co-N₂C₂ with axial Au atom moieties act as the active sites of the (Au-Co) dual atoms towards ORR. Further, *OH adsorbed on the Co atom induces a coordinated change in the adjacent Au atom symmetry, which leads the anti-bond spin orbitals to a low energy level, thus, further improving ORR performance. The development of (Au-Co) dual atoms via the regulation of d-orbitals symmetry provides an encouraging way to design highly efficient (electro)catalysts.

1. Introduction

The supported metal nano-electrocatalysts exhibit a significant promise in the electrochemical energy conversion technologies owing to their large-scale production and selective product formation [1–5]. Nevertheless, a limited three-dimensional surface accessibility of the loaded nanoparticles leads to a low degree of atom utilization and enhanced mass-transfer resistance [6–9]. In addition, high compositional and structural inhomogeneity of the heterogeneous catalysts strongly hinders the understanding of the reaction mechanism at the atomic-scale, thus, making the exposure of more active centers difficult [10–12]. The single metal atom (SAs), a dramatic class of catalysts, integrate the advantages of the heterogeneous and homogenous catalysts, including 100% atom utilization, high stability and excellent recyclability, thus arousing an extensive research interest [13–18]. The well-defined structure of SAs makes them an ideal model for unraveling the chemical processes associated with the given active centers [19–23].

Besides, SAs with highly unsaturated coordination and unique electronic structure endow a superior performance in many (electro)catalytic processes [24–29]. However, a relatively slow activation of the multi-molecules on SAs owing to their structural simplicity and absence of the resemble sites limit the application of SAs [30–33].

Compared with SAs, the dual metal atoms not only exhibit the same merits [34–37], but also demonstrate the synergistic effect and resemble sites, thus, benefitting the activation of the complex molecules [12, 38–41]. The synergistic interaction of the dual metal atoms is mainly determined by their chemical nature, which controls the structure of the d-orbitals owing to the difference in the localized d-electron density and atomic coordination symmetry [42,43]. Both dual precious metal atoms (DPAs) and dual non-precious metal atoms (DNPAs) have been fabricated and reported to exhibit significantly enhanced activity and stability [44–48], in comparison with their single metal atom counterparts. The non-precious metal atoms, such as Fe, Co and Ni, exhibit mutable spin d orbital configurations in the local coordination environments,

* Corresponding authors.

E-mail addresses: jiajunhit@hit.edu.cn (J. Wang), liminliu@buaa.edu.cn (L.-M. Liu), xsun9@uwo.ca (X. Sun).

¹ These authors contributed equally: Fanpeng Kong, Rutong Si.

which strongly affect the catalytic reactivity [34,49,50]. Further, the d orbitals of the precious metals exhibit high locality and weak electronic interaction with the adsorbed catalytic intermediates [51]. It is suggested that the adsorption on the active sites of the precious SAs is strongly affected by the intrinsic property of the d orbitals [52–54]. Therefore, the hetero-nuclear precious-non-precious dual atoms (DP-NPAs) are expected to reveal the extraordinary d-electron spin configurations, thus, endowing excellent activity, stability and selectivity, which are different from those of DPAs and DNPAs. However, DP-NPAs with effective electro-catalytical performance are still in fancy.

Herein, the novel (Au-Co) DP-NPAs have been successfully synthesized to boost the acidic ORR kinetics as the strong coupling between the fully filled d orbitals of the Au atom and spin d orbitals of the Co atom can strengthen the chemical interaction between the reagents and active centers. (Au-Co) DP-NPAs consisting of Co-N₂C₂ with the axial Au atom moieties have been observed to achieve an excellent activity with E_{1/2} of 0.82 V and high selectivity for the four-electron pathway in an acid solution, thus, leading to the classification as one of the most optimal Co-based catalysts. The remarkable ORR activity on (Au-Co) DP-NPAs is also demonstrated in the PEM fuel cells with a peak power density of 360 W cm⁻² under 1 bar H₂/air condition. The significantly enhanced stability on (Au-Co) DP-NPAs is demonstrated by a negligible 15-mV decline in the E_{1/2} value after 30,000 potential cycles. Furthermore, the mechanistic details of ORR on (Au-Co) DP-NPAs has been revealed by the density functional theory (DFT) calculations.

2. Experimental section

2.1. Preparation of electrocatalysts

2.1.1. Preparation of (Au-Co) DP-NPAs

In a normal procedure, Zn(NO₃)₂·6H₂O, Co(NO₃)₂·6H₂O, and HAuCl₄·3H₂O was dissolved in 200 mL methanol, which was poured into 200 mL methanol containing 4.0 g 2-methylimidazole. The above-mixed solution was heated at 60 °C for 24 h. The obtained precipitates were centrifuged and washed with ethanol for three times and dried in vacuum at 60 °C for 12 h. 300 mg powder was placed into a tube furnace and precursors were pyrolyzed at 1000 °C for 1 h in Ar atmosphere to obtain (Au-Co) DP-NPAs.

2.1.2. Preparation of Co SAs

The synthetic process in the case of Co SAs is similar to (Au-Co) DP-NPAs except the use of chloroauric acid.

2.1.3. Preparation of Au SAs

The synthetic process in the case of Au SAs is similar to (Au-Co) DP-NPAs except the use of cobalt nitrate hexahydrate.

2.1.4. Preparation of N-C

The synthetic process in the case of N-C is similar to (Au-Co) DP-NPAs except the use of cobalt nitrate hexahydrate and chloroauric acid.

2.1.5. Preparation of Au NPs/Co SAs

The synthetic process in the case of Au NPs/Co SAs is similar to (Au-Co) DP-NPAs except the use of two-fold chloroauric acid content.

2.2. Physical characterization

Scanning electron microscopy was carried out on high-resolution field-emission scanning electron microscopy (Hitachi 4800). Transmission electron microscopy (TEM), high-resolution TEM (HR-TEM), and high angle annular dark field-scanning transmission electron microscopy (HAADF-STEM) were carried out on FEI Tecnai G2F30 with an acceleration voltage of 300 kV. Atomic resolution- HAADF-STEM images were collected on double Cs-corrected FEI Titan Themis G2 operating at 300 kV equipped with an X-FEG gun and Bruker Super-X EDX detectors.

The STEM-EDX mapping was obtained with a beam current of ~1 nA and counts up to 6k cps for ~5 min. Cu grids were used during all the EDS analyses. The metal content was determined by a PerkinElmer Optima 5300DV inductively coupled plasma (ICP) instrument. Surface area and pore distribution analysis of samples were tested by N₂ adsorption/desorption at 77 K with an Autosorb-IQ Gas sorption system. X-ray photoelectron spectroscopy (XPS) was performed on a PHI 5700 ECSA system using Al Kα radiation (1486.6 eV). Powder X-ray diffraction (XRD) was carried out on a Rigaku D/max-γA X-ray diffractometer with Cu Kα radiation (λ = 1.54178 Å). Raman spectra were performed using a Renishaw Raman system at 514 nm excitation. The hard X-ray micro-analysis (HXMA) beamline (Canadian Light Source) and the beamline 20-BM-B at the Advanced Photo Source (APS, Argonne National Laboratory) were used to obtain the Co K edge and Au L₃ edge spectrum. Each spectrum was collected under the fluorescence yield mode with a solid-state detector. The Co foil, CoPc, and Au foil spectra were also collected under transmission mode for comparison and energy calibration. In EXAFS R space curve fitting, software Athena was used for data reduction, Feff7.02 used for theoretical calculation in phase and amplitude for the XAFS backscattering, and Win XAS used for R space curve fitting.

2.3. Electrochemical measurements

4 mg catalyst was dispersed in a solution of 400 μL isopropanol and 40 μL Nafion by sonication for 10 min (10 mg mL⁻¹). The catalyst ink was dropped on a polished rotating ring disk glassy carbon electrode (5.6 mm in diameter) and the loading of PGM-free is 0.8 mg cm⁻². The ink for Pt/C was prepared through dispersing 4 mg catalysts into the mixture of 3 mL deionized water, 1 mL isopropanol, and 4 μL Nafion, followed by ultrasonic dispersion. And the Pt loading on the work electrode is 60 μg cm⁻². Graphite rod and Ag/AgCl were used as the counter electrode and reference electrode, respectively. Cyclic voltammetry (CV) curves were recorded in argon saturated 0.1 M HClO₄ solution at a scan rate of 50 mV s⁻¹. The oxygen reduction performance was tested by linear sweep voltammogram using a rotating ring disk electrode in oxygen saturated 0.1 M HClO₄ solution at a rotation rate of 900 r min⁻¹ (scan rate = 10 mV s⁻¹). The accelerated stress tests (ASTs) were performed by applying 30,000 potential cycles between 0.6 V and 1.0 V at a scan rate of 50 mV s⁻¹ in oxygen saturated 0.1 M HClO₄ solution. Besides, chronoamperometry at high potential oxygen saturated 0.1 M HClO₄ solution was also carried out to evaluated stability. All the electrochemical measurements were conducted on a CHI 760E electrochemical workstation at room temperature, and the potentials were reported with respect to the reversible hydrogen electrode (RHE). The H₂O₂ yield and transfer electron number were determined by the following equation:

$$\%H_2O_2 = \frac{200I_R/N}{I_D + (I_R/N)}$$

$$n = \frac{4I_D}{I_D + (I_R/N)}$$

Where I_D is the Faradaic current at disk electrode, I_R is Faradaic current at the ring electrode and N is the H₂O₂ collection coefficient at the ring. The transfer electron number during ORR was also determined by the Koutechy-Levich (K-L) equation as follows:

$$\frac{1}{j} = \frac{1}{j_L} + \frac{1}{j_k} = \frac{1}{B\omega^{1/2}} + \frac{1}{j_k}$$

$$B = 0.62nFC_0D_0^{2/3}v^{-1/6}$$

Where j is the measured current, j_k is the kinetic current and j_L is the diffusion limiting current, n is the transfer electron number, F is the Faraday constant (96,500 C mol⁻¹), C₀ is the bulk concentration of O₂

($0.0012 \text{ mol L}^{-1}$), D_0 is the diffusion coefficient of O_2 ($1.9 \times 10^{-5} \text{ cm}^2 \text{ s}^{-1}$) and ν is the kinetic viscosity of the electrolyte ($0.01 \text{ cm}^2 \text{ s}^{-1}$).

2.4. Fuel cell tests

The catalysts were ultrasonically dispersed into the mixture of de-ionized, isopropanol, and 5% Nafion suspension. The inks were applied to a gas diffusion layer (GDL) by ultrasonic spraying until the cathode catalyst loading of 4.0 mg cm^{-2} was achieved. The inks containing commercial Pt/C were sprayed onto decals until the catalyst loading of $0.1 \text{ mg}_{\text{Pt}} \text{ cm}^{-2}$ was reached. The membrane electrode assembly with the geometric area of 5.0 cm^2 was fabricated through hot-pressing cathode and anode onto the Nafion 212 membrane. Fuel cell testing was carried out in a single-cell fuel cell with straight parallel flow channels. Fuel cell polarization curves were recorded in a constant-current mode at 100% RH and 80°C under $1.0 \text{ bar H}_2/\text{O}_2$ and $1.0 \text{ bar H}_2/\text{air}$.

2.5. First-principles calculations

Computational method. We performed first-principles calculations by the CP2K/Quickstep package [55]. The Perdew–Burke–Ernzerhof (PBE) functional was used to describe the correlation energies and nonlocal exchange [56]. The norm-conserving Goedecker, Teter, and Hutter (GTH) pseudopotentials were used to describe core electrons [57]. Gaussian function with molecularly optimized double-zeta polarized basis sets (m-DZVP) were adopted for expanding the wave function of N $1s^2 2s^2 2p^3$ and C $1s^2 2s^2 2p^2$, and triple-zeta polarized basis sets (m-TZVP) for H $1s^1$, Au $5d^{10} 6s^1$ and Co $3d^7 4s^2$ electrons [58]. A 500 Ry cut-off energy was used for auxiliary basis set of plane waves. During the calculations, all the atomic positions were fully relaxed until the force is smaller than 0.05 eV/\AA . The self-consistent continuum solvation model were applied to capture the water effects [59].

The catalytic activity for ORR. The ORR activity was calculated using the method introduced by Nørskov, in which the free energy of all in-

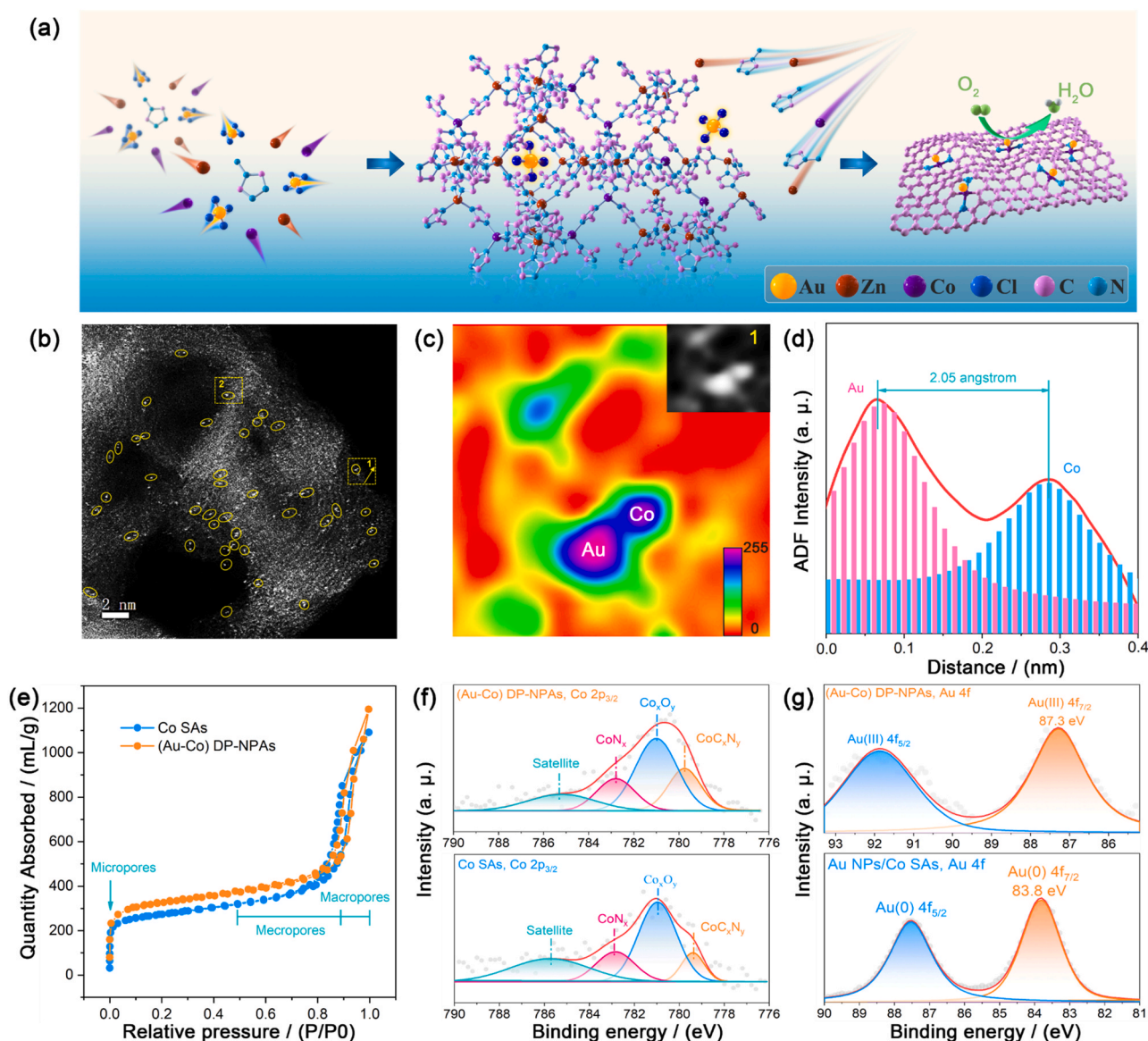
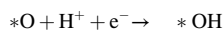
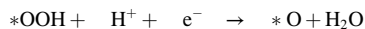
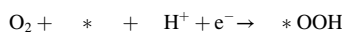


Fig. 1. Synthesis and characterization of (Au-Co) DP-NPAs. (a) The schematic diagram for the fabrication of (Au-Co) DP-NPAs. (b) Aberration corrected-HAADF-STEM image of (Au-Co) DP-NPAs. (c) The colored raster graphic of Region 1 in Fig. 1b. (d) The intensity profile along the arrow in Region 1 of Fig. 1b. (e) The nitrogen adsorption-desorption isotherms of Co SAs and (Au-Co) DP-NPAs measured at 77 K. (f) High-resolution XPS spectra for Co SAs and (Au-Co) DP-NPAs taken at the binding energy of Co 2p_{3/2}. (g) High-resolution XPS spectra for (Au-Co) DP-NPAs and Au NPs/Co SAs taken at the binding energy of Au 4f_{7/2}.

intermediates can be obtained from first-principles DFT calculations. The associative mechanism was carried out, in which the reaction in acidic solution is given by the elementary steps:



For each electron-transfer step, the free energy change (ΔG) can be expressed as follows:

$$\Delta G = \Delta E + \Delta \text{ZPE} - T\Delta S - eU$$

Here, the ΔE , ΔZPE , $T\Delta S$, and U represent the energy changes, zero-point energy correction, entropic energy, and the applied potential vs. RHE, respectively.

3. Results and discussion

3.1. Synthesis and Characterization of (Au-Co) DP-NPAs

(Au-Co) DP-NPAs were synthesized by combining the host-guest and chemical doping strategies, as shown in Fig. 1a. The Co-doped zeolitic imidazolate frameworks-8 hosting tetrachloroaurate (Au/Co-ZIF8) was subjected to pyrolysis at 1000 °C in an Ar atmosphere to obtain the atomically dispersed Au-Co pairs. During this process, Zn was volatilized due to its low boiling point (907 °C) [60,61], while the cobalt nodes and hosted tetrachloroaurate evolved into the dual atoms anchored on the carbonized carbon matrix (Fig. S1). The scanning (SEM) and transmission (TEM) electron microscope images of (Au-Co) DP-NPAs in Fig. S2a and S2b reveal a highly uniform rhombic dodecahedron morphology, with a narrow size distribution and an average particle size of ~ 60 nm. The absence of the metal clusters and nanoparticles is demonstrated in the high angle annular dark field – scanning transmission electron microscopy (HAADF-STEM) image (Fig. S2c). The aberration-corrected HAADF-STEM image with sub-angstrom resolution further elucidates the atomic dispersion of Co and Au on the carbonized porous carbon (Fig. S3). A number of atomic pairs with varying brightness are observed (marked with yellow circles in the high magnification image, Fig. 1b), thus, indicating the formation of the (Au-Co) atomic pairs based on the obvious Z-contrast between Au ($Z = 79$) and Co ($Z = 27$). The representative isolated dual-metal pairs at the edge of the carbon matrix in Region 1 and Region 2 in Fig. 1b are directly evidenced in the raster graphic (Fig. 1c and Fig. S4). Also, the intensity profile of the atomic pair in Region 1 reveals the presence of a diatomic feature, with a bond length of 2.05 Å (Fig. 1d). The elemental distribution in (Au-Co) DP-NPAs analyzed through EDS-mapping (Fig. S5) exhibits a high homogeneity for all elements in the three-dimensional carbon architecture. As observed, an increment in the Au precursor content leads to the formation of the small-sized gold particles, denoted as Au NPs/Co SAs (Fig. S6). To explore the communicative effect of (Au-Co) DP-NPAs, Co SAs were also prepared using the similar synthesis strategy for comparison, and the corresponding electron microscope images are shown in Figs. S7-S9.

The X-ray diffraction (XRD) pattern of (Au-Co) DP-NPAs (Fig. S10) exhibits a broad shoulder peak, attributed to the contribution of the amorphous carbon and absence of nanocrystals, in compliance with the atomic dispersion. The N_2 adsorption/desorption analysis exhibits the similar Brunauer-Emmet-Teller (BET) surface area and pore size distribution for both (Au-Co) DP-NPAs and Co SAs (Fig. 1e, Fig. S11, and Table S1). The X-ray photoelectron spectroscopy (XPS) and inductively coupled plasma optical emission spectrometer (ICP-OES) also reveal the similar content of Co species in (Au-Co) DP-NPAs and Co SAs (Table S2). Except for the compositional information, the structural and

environmental information of the local surface has been revealed through high-resolution XPS, as shown in Fig. S12 and Table S3-S5. The N 1s spectrum of (Au-Co) DP-NPAs, similar to that of Co SAs, can be deconvoluted into four peaks. The peak at ~399.5 eV is assigned to the N-metal (Fig. S12d) [61,62]. The presence of the deconvoluted Co-N peak (782.9 eV) in the Co 2p XPS spectrum (Fig. 1f) also demonstrates the coordination between Co and N in (Au-Co) DP-NPAs, thus, revealing the presence of the atomically dispersed metal atoms, in line with the findings from the atomic resolution HAADF-STEM images. Besides, the Au 4f_{7/2} XPS peak at 87.3 eV in the case of (Au-Co) DP-NPAs indicates the Au (III) chemical state rather than the metallic state which is observed in Au NPs/Co SAs (Fig. 1g).

3.2. Identification of active sites of (Au-Co) DP-NPAs by XAS fitting and DFT calculations

To obtain the molecular-scale insights into the electronic and coordinative environments of (Au-Co) DP-NPAs, the synchrotron radiation-based X-ray absorption near edge structure (XANES) and extended X-ray absorption fine structure (EXAFS) analysis were performed for (Au-Co) DP-NPAs along with the Co foil and cobalt phthalocyanine (CoPc) as the reference materials. The Co K edge absorption energy in the case of (Au-Co) DP-NPAs is observed to be located between those of Co foil and CoPc, as shown in the inset of Fig. 2a. It suggests that the Co atoms are positively charged, and the oxidation valence is between Co⁰ and Co^{II}. Besides, the positive shift of the Co K absorption edge in (Au-Co) DP-NPAs indicates a high extent of Co^{δ+} oxidation, [63] possibly brought about by the adjacent Au atom. The Fourier transforms (FT) k²-weighted $\chi(k)$ -functions of Co EXAFS for (Au-Co) DP-NPAs are shown in Fig. 2b. The prominent FT peak at about 1.4 Å in the EXAFS R space is attributed to the contribution of the nearest neighbor coordination associated with the Co-N/C first-shell. Besides, the absence of the metallic Co-Co scattering path corresponding to the FT peak at 2.10 Å (green trace, Fig. 2b) demonstrates an atomic dispersion in (Au-Co) DP-NPAs. Further, the unusual double peak at the low R data range is only observed for (Au-Co) DP-NPAs, which may possibly arise due to a new scattering path. The absence of the metallic Co-Co path with an intensity maximum at $k = 6.8 \text{ \AA}^{-1}$ in the wavelet transform (WT) of the EXAFS oscillation also corroborates the atomic dispersion (Fig. 2c and Fig. S13).

XANES and EXAFS were also employed to investigate the chemical and structural information of Au in (Au-Co) DP-NPAs. For (Au-Co) DP-NPAs, the white-line peak of Au L₃ edge XANES (Fig. 2d) displays a sharp white-line feature. In comparison, almost no white-line feature is observed in the Au foil owing to the filled 5d state of Au⁰, thus, suggesting a significantly different electronic and atomic environment in (Au-Co) DP-NPAs [64]. Further, the Au (III) in (Au-Co) DP-NPAs is revealed by comparing the XANES spectra (Fig. S14) and is observed to be in line with the XPS findings. Also, the widened simple sine oscillation is observed at Au L₃ edge for (Au-Co) DP-NPAs rather than the periodic oscillation, thus, suggesting the absence of the long-range ordered Au local structure in (Au-Co) DP-NPAs. The FT k²-weighted $\chi(k)$ -functions of Au L₃ edge EXAFS for (Au-Co) DP-NPAs and Au foil are presented in Fig. 2e. The absence of the peak attributed to the Au-Au first-shell (metallic Au) demonstrates the atomic dispersion of the Au sites. In contrast with the WT-EXAFS spectrum of the Au foil (Fig. 2f), the k value at the maximum intensity in the contour line for (Au-Co) DP-NPAs is about 4 \AA^{-1} , thus, supporting the absence of the Au-Au first-shell. Based on the findings from XAFS and aberration-corrected HAADF-STEM, the presence of the atomically dispersed Au-Co atomic pairs is unambiguously confirmed. In addition, Au NPs/Co SAs also exhibit the presence of the metal-state Au nanoparticles, as confirmed from the XANES and EXAFS spectra (Fig. S15).

The quantitative structural parameters of the Co and Au atoms in (Au-Co) DP-NPAs have been extracted by fitting the least-squares EXAFS R space curve based on a structural model, including Co-C, Co-N and Co-Au scattering paths with the coordination numbers of 2, 2 and 1,

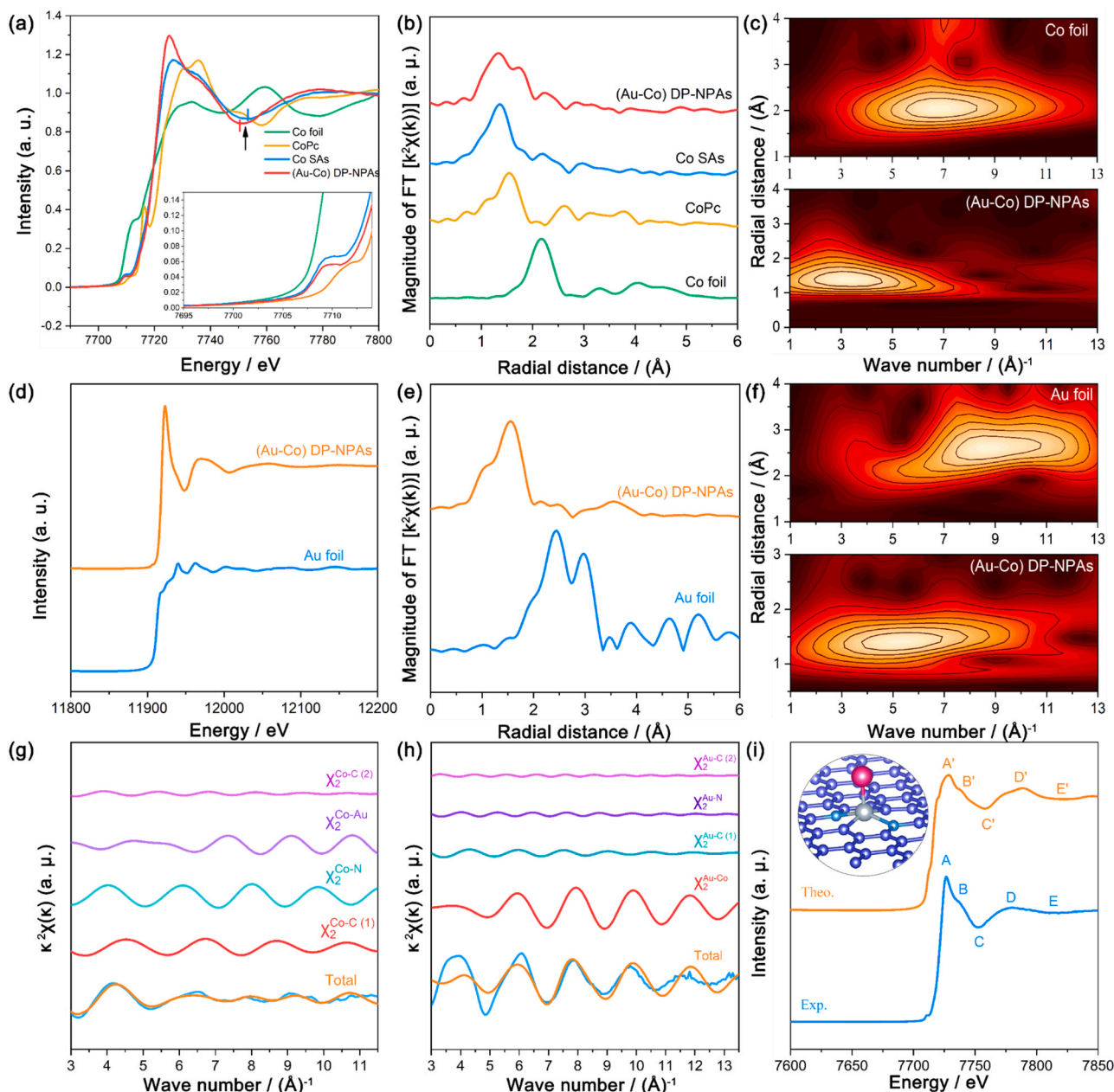


Fig. 2. XAS characterization of (Au-Co) DP-NPAs. Normalized Co K-edge XANES (a) and EXAFS (b) spectra of Co foil, CoPc, Co SAs, and (Au-Co) DP-NPAs. (c) Wavelet transforms for the k^2 -weighted Co K-edge EXAFS signal of Co foil and (Au-Co) DP-NPAs. Normalized Au L-edge XANES (d) and EXAFS (e) spectra of Au foil and (Au-Co) DP-NPAs. (f) Wavelet transforms for the k^2 -weighted Au L-edge EXAFS signal of Au foil and (Au-Co) DP-NPAs. A comparison made for $k^2\chi(k)$ between experimental data and R space fitting based on total Feff modeling and each scattering path for Co K-edge (g) and Au L-edge (h). (i) The comparison between experimental XANES spectrum and the best-fit of Co K-edge XANES modeling for (Au-Co) DP-NPAs. The inset is proposed architecture of (Au-Co) DP-NPAs consisted of centrosymmetric CoN₂C₂ with axial Au atom.

respectively. The model has been developed based on the DFT predictions for the Au-Co atomic pairs. The besting Feff fitting analysis of (Au-Co) DP-NPAs shows the presence of Co-C, Co-N and Co-Au scattering paths with the coordination numbers of 2.1, 2.2 and 0.9, respectively, in agreement with the DFT predictions (Fig. 2g, Fig. S16, and Table S6). DFT has also been used to deduce the possible configuration of the Au atoms based on EXAFS and Feff fitting curve (Fig. 2h, Fig. S17, and Table S6). The fitting analysis reveals the presence of the Au-Co coordination with the coordination number of 1.1 and bond length of 1.93 Å. It further confirms the validity of the DFT analysis for exploring the local Au structure environment. The fitting results of the Co K edge and Au L₃ edge corroborate with each other, thus, supporting the Au-Co atomic pair configuration predicted by DFT. The mono-

dispersed CoN₂C₂ moieties are observed to prevail in Co SAs with a lack of the Co-Co coordination path (Fig. S18 and Table S7). Also, the local coordinative information for the Co and Au foils, derived from the Feff fitting of EXAFS, has been shown in Fig. S19-S20 and Table S8 for reference.

To further verify the local structure of (Au-Co) DP-NPAs, the DFT guided theoretically calculated Co K edge XANES spectra has been conducted by using the FDMNES codes, which is highly sensitive to the 3D atomic arrangement around the photo-absorber. The calculated XANES spectra exhibit similar peak features as the experimental results (Fig. 2i and Fig. S21), consistent with the EXAFS R space curve fitting. For further comparison, the theoretically calculated XANES spectra based on other DFT models are shown in Fig. S22. Combining the EXAFS

fitting, XANES simulations and DFT calculations, the atomic-site structure of (Au-Co) DP-NPAs has been identified as Co-N₂C₂ with the axial Au atom moieties (Fig. 2i inset). The in-depth analysis suggests that the presence of the axial Au atom leads to a more positively charged Co atom and elongation of the Co-C(N) bond in (Au-Co) DP-NPAs in comparison with Co SAs.

3.3. Electrocatalytic performance of (Au-Co) DP-NPAs towards ORR in acid medium

The ORR activity and selectivity of (Au-Co) DP-NPAs are evaluated using a rotating ring disk electrode (RRDE) in an oxygen saturated acid electrolyte. The best performing (Au-Co) DP-NPAs after the optimization of pyrolysis temperature and content of the Co and Au precursor (Fig. S23-S25) exhibit a significant ORR activity with the onset potential (E_{onset}) and $E_{1/2}$ of 0.918 V and 0.820 V, respectively (Fig. 3a,b, and Fig. S26). It is worth noting that there is nearly no ORR activity on Au SAs, even though their synthesis has been carried out by employing the similar approach, except the introduction of the Co species. Besides, it is

also found Au NPs/Co SAs exhibit an inferior activity as compared to (Au-Co) DP-NPAs (Fig. S23). Therefore, the observed 25-mV enhancement in $E_{1/2}$ for (Au-Co) DP-NPAs in comparison with Co SAs is likely associated with the synergistic role of the (Au-Co) dual atoms, as observed from the combined aberration-corrected HAADF-STEM and XAFS. The performance of (Au-Co) DP-NPAs is noted to be lower than that of Pt/C by only 30 mV. Further, the performance is comparable to a majority of Fe-based catalysts (Table S9) as well as exceeds a majority of most Co-based catalysts (Fig. 3c), such as (Zn-Co) DNPAs [48], (Co-Co) DNPAs [47], and (Fe-Mn) DNPAs [43]. In addition to $E_{1/2}$, the mass activity at 0.85 V calculated by dividing the kinetic current with the metal mass also represents a vital criterion. Mass activity for (Au-Co) DP-NPAs is noted to be 1.95 and 1.30 times higher as compared with that of Co SAs and Pt/C, respectively, thus, suggesting that the synergistic effect significantly boosts the ORR activity (Fig. 3b). The Tafel plots (Fig. 3d) also confirm the superb ORR activity of (Au-Co) DP-NPAs with the slope value of 69 mV dec⁻¹. The H₂O₂ yield on (Au-Co) DP-NPAs is noted to be substantially reduced over the potential range from 0.8 V to 0.2 V, which is observed to be much lower than Co SAs

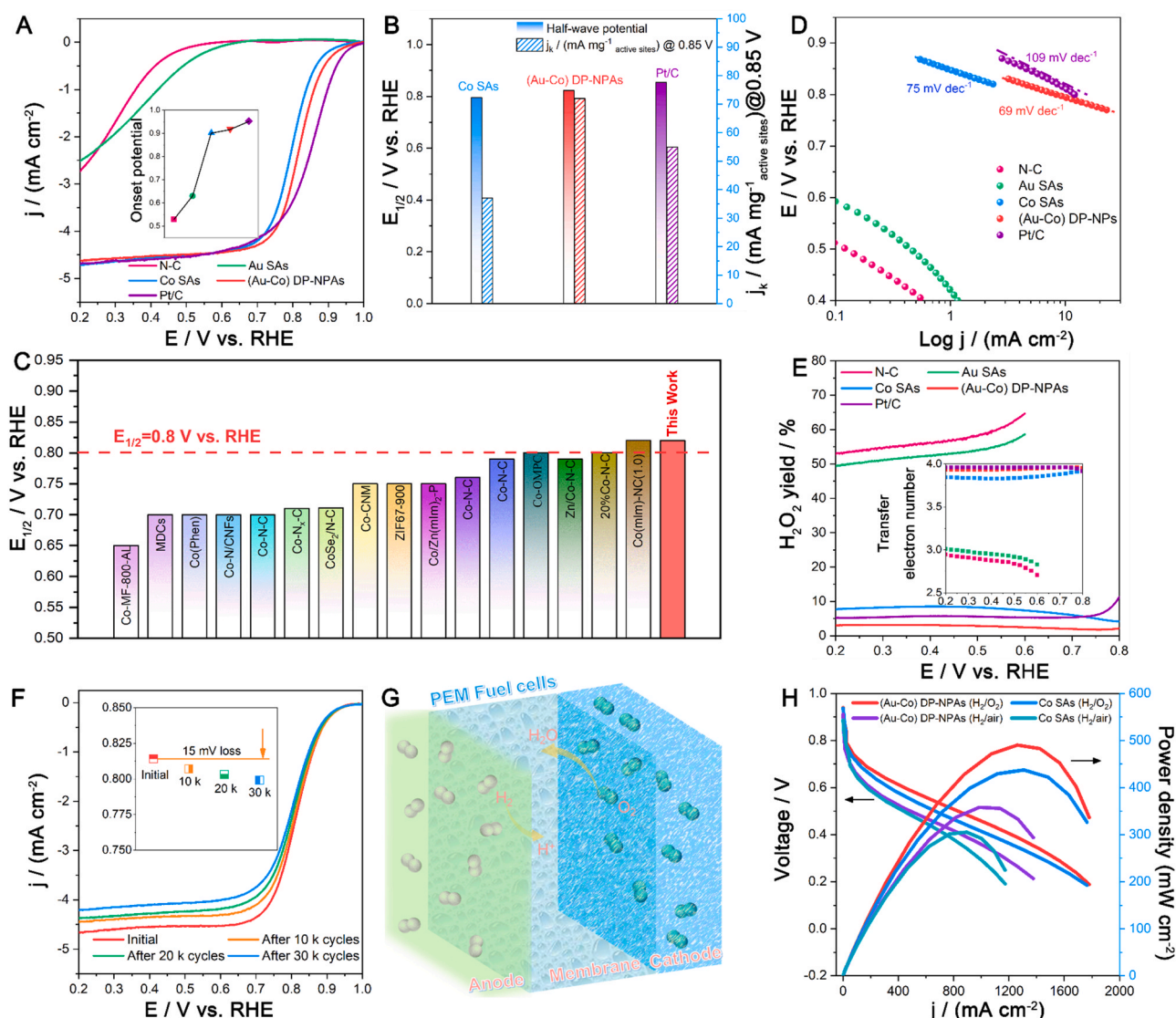


Fig. 3. Electrocatalytic performance of (Au-Co) DP-NPAs towards ORR. (a) Linear sweep voltammograms of (Au-Co) DP-NPAs in oxygen saturated 0.1 M HClO₄ at a rotation rate of 900 r min⁻¹ (scan rate = 10 mV s⁻¹). (b) The bar chart of half-wave potential and mass activity at 0.85 V for Co SAs, (Au-Co) DP-NPAs, and Pt/C. (c) The half-wave potential of other recently published Co-based catalysts and (Au-Co) DP-NPAs. (d) Tafel curves for (Au-Co) DP-NPAs. (e) H₂O₂ yield and transfer electron number for Co SAs and (Au-Co) DP-NPAs. (f) The polarization curves of (Au-Co) DP-NPAs in oxygen saturated 0.1 M HClO₄ after ASTs with different cycles. (g) Schematic diagram of PEM fuel cells. (h) MEA performance of (Au-Co) DP-NPAs and Co SAs at 100% RH under 1 bar H₂/O₂ and 1 bar H₂/air condition.

(Fig. 3e). Besides, the findings from the K-L plot are also in line with the much-improved selectivity observed for (Au-Co) DP-NPAs (Fig. S27 and S28).

The long-term stability is another pivotal criterion for evaluating the ORR catalysts and has been studied by employing two accelerated stress tests (ASTs) protocols, including dynamic potential cycle and chronoamperometry in oxygen saturated acid electrolyte. (Au-Co) DP-NPAs exhibit a significantly enhanced stability, with only a 15-mV negative shift in $E_{1/2}$ after 30,000 potential cycles, as compared to a loss of 29 mV and 34 mV in $E_{1/2}$ for Co SAs and Pt/C, respectively, as shown in Fig. 3f and Fig. S29. Furthermore, the excellent stability of (Au-Co) DP-NPAs is also supported by the chronoamperometry analysis carried out to simulate the real fuel cell operation condition (Fig. S30 and S31). The similar Raman spectra, electrochemical impedance spectra (EIS) and CV profiles of (Au-Co) DP-NPAs and Co SAs after ADTs suggest the almost same corroded carbon matrix, which is not affected by the synergistic role of the dual atoms (Fig. S32, S33 and Table S10). The enhanced stability of (Au-Co) DP-NPAs may stem from the relatively stable active centers resulting from the strong coupling interaction between the spin d orbitals of the Co atom and fully filled d orbitals of the Au atom (Fig. S33).

(Au-Co) DP-NPAs have been further tested in the actual PEM fuel cells to explore their feasibility as the practical PGM-free cathodes (Fig. 3g). 5 cm² MEAs with a PGM-free catalyst loading of 4 mg cm⁻² are first tested in the H₂/O₂ fuel cell to minimize the mass-transfer resistance, so as to accurately study the true catalytic activity in the fuel cell environment. At 1 bar H₂/O₂ condition (Fig. 3h), the fuel cell

employing (Au-Co) DP-NPAs as the cathode catalyst achieves a current density of 148 mA cm⁻² at 0.7 V and a peak power density of 490 mW cm⁻², which exceed those of the corresponding Co SAs. Also, under more practical 1 bar H₂/air conditions, the (Au-Co) DP-NPAs-based cathode also generates a peak power density of 360 mW cm⁻² (Fig. 3h), which represents the best performance among the non-Fe PGM-free catalysts-derived H₂-air fuel cells (Table S11). The significantly enhanced fuel cell performance in the case of (Au-Co) DP-NPAs can be rationally attributed to the unique precious-non-precious Au-Co active centers.

3.4. Catalytic mechanism by DFT calculations

First-principles calculations have been performed to explore the origin of greatly enhanced acidic ORR activity on (Au-Co) DP-NPAs. Considering that the Co-ZIF8 is synthesized prior to the formation of (Au-Co) DP-NPAs, the Co atoms should be coordinated by the nitrogen and carbon atoms. Besides, the centrosymmetric Co-N₂C₂ with the axial Au atom moieties have been revealed through XANES, EXAFS and DFT analyses. Thus, the subsequent first-principles calculations have been performed using the Au-Co dual atoms on the N-doped graphene with two nitrogen atoms coordinated to the Co atoms.

The adsorption of the oxygenous intermediates on (Au-Co) DP-NPAs is further examined so as to explore the ORR pathway. As shown in Fig. 4a, the O₂ molecule is adsorbed on the Au side of (Au-Co) DP-NPAs. The O₂ molecule is subsequently converted to *OH after the reduced electron-proton reaction. ORR is completed once *OH desorbs from the Au site.

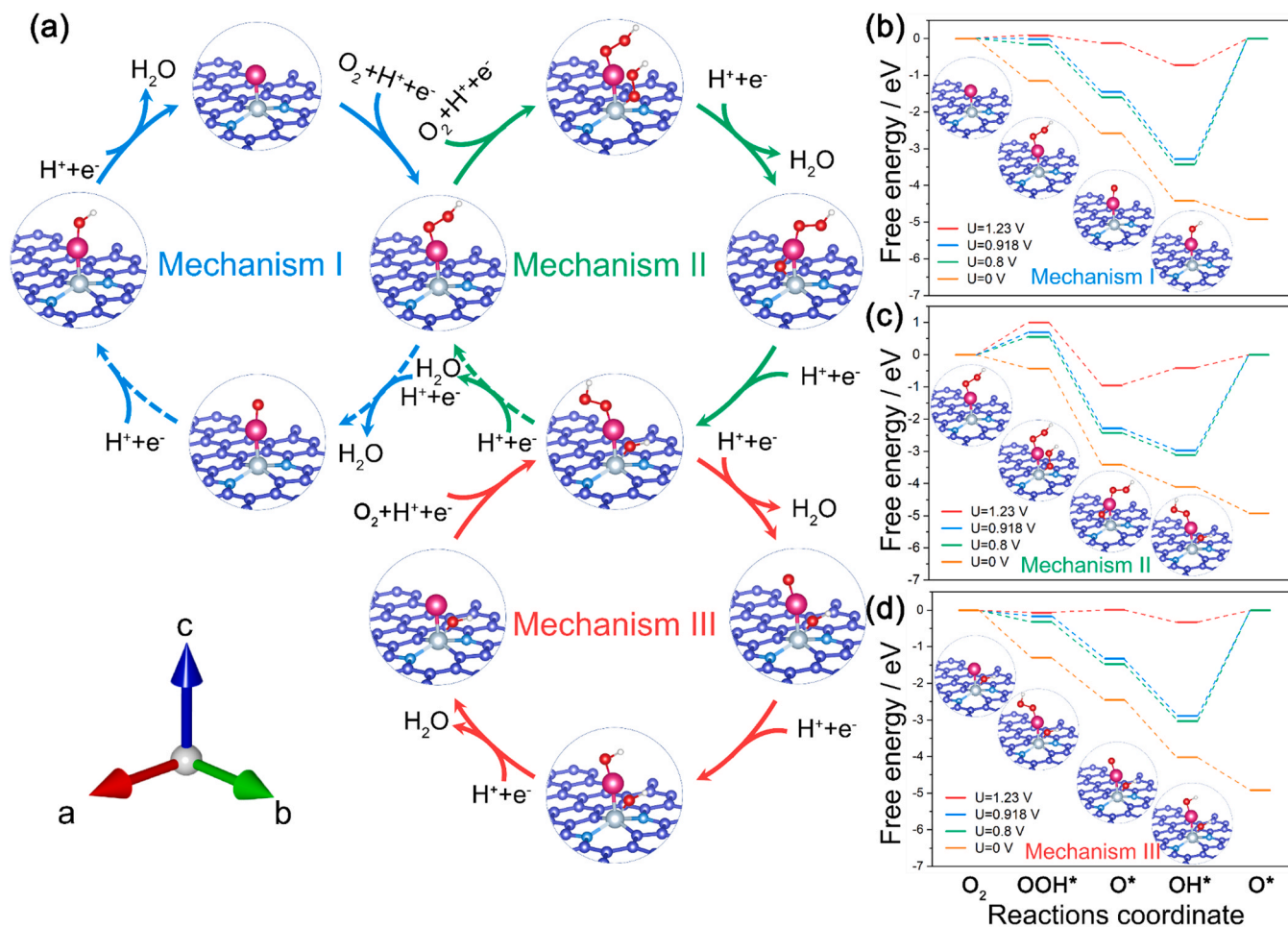


Fig. 4. The diagram of the ORR pathway and corresponding Gibbs free energy. (a) Oxygenous intermediates configurations on the (Au-Co) DP-NPAs during the ORR pathway, dash lines represent the energy-unfavored reaction pathways. (b) The diagram of ΔG for three reaction mechanisms. The Mechanism III indicated by red circle represents the final ORR circle. pink, grey, light blue, dark blue, red, white balls represent the Au, Co, N, C, O, H atoms, respectively.

The corresponding Gibbs free energy diagrams for the ORR process are shown in Fig. 4b. It is found that the free energy difference (ΔG) for each step is downhill under the potential of 0.918 V, except for the step involving the formation of $^*\text{OOH}$. This step is non-spontaneous step at 0.918 V, which indicates that it can only provide electric potential under 0.918 V under mechanism I. As mentioned earlier, an activated electric circle is performed, which is needed to react with the $^*\text{OOH}$ adsorbed on the Au side acting as the active intermediate for mechanism II.

In the presence of adsorbed $^*\text{OOH}$ on the Au atom, the Co atom also adsorbs the oxygenous intermediates under mechanism II, as shown in Fig. 4a. The corresponding ΔG of the first step of mechanism II is remarkably inclined, which reveals an electric potential lower than 0.918 V under mechanism II. However, it can react with an active configuration under mechanism III to attain the best ORR performance (Fig. 4a). As $^*\text{OH}$ is adsorbed on the Co atom, the ORR reaction site shifts to the Au atom. The corresponding ΔG is downhill at a potential of 0.918 V, which indicates that the over-potential of ORR under mechanism III is lower than 312 mV, which coincides with the experimental results. The calculated overpotential with including the solvation effect is slightly increased by 0.18 V, while it shows the same mechanism for both without and with considering the solvent effect. Comparing with mechanism I and II, the rate-determining step is always noted to be the $^*\text{OOH}$ adsorption step. The adsorbed species on Co the atoms exhibit a major difference, which indicates that the adsorbed species on the Co atom should be the key point for exploring the ORR performance.

To study the extraordinary improvement in the ORR catalytic activity by the $^*\text{OH}$ adsorbed on the Co atoms, the corresponding projected density of states (PDOS) and molecular orbital of the Au and Co atoms in (Au-Co) DP-NPAs has been examined based on the d-orbital configuration and atomic coordination symmetry. The corresponding PDOS are

shown in Fig. 5a. Notably, in case different species are adsorbed on the Co atom, the Au atom mainly heads to the z orientation and interacts with the d_{z^2} orbital of the Co atom. Several literature studies reveal that the d orbital leads to splitting and unoccupied spin-orbital due to the coordination transformation introduced by the coordination of the N and adsorbed atoms [65,66]. The d orbitals construct the base of a symmetry group and form different irreducible representations under the symmetry group induced by the coordinated atoms. Some previous works reveal that metallic atoms tend to be oxidized state, which means the anti-bond state is mostly made up of the unoccupied d-orbitals of metallic atoms [61]. The coordinated symmetry of Au is consistently C_{2v} prior to the $^*\text{OH}$ adsorption on the Co atom. In the absence of any adsorbent on the Co atom, the corresponding coordinated symmetry group is mainly D_{3h} . The d_{z^2} orbital belonging to the A_1 irreducible representation is quite high and interacts with the Au atom. The p orbital of the oxygen atom of $^*\text{OOH}$ has a weak interaction with the $d_{x^2-y^2}$ orbital of the Au atom. Thus, it is not easy to adsorb $^*\text{OOH}$ on Au atom. In case $^*\text{OOH}$ and $^*\text{OH}$ are adsorbed on the Co atom, the interaction between the Au and Co atoms weakens due to the charge transfer of the adsorbents and metal atoms (Table S12). It is embodied by the Au–Co bond length, as shown in Table S13, thus, the atomic coordinated symmetry is noted to change. The corresponding coordinated symmetry groups are D_{2d} and D_{4h} and the d_{z^2} orbital belongs to the A_1 and A_1g irreducible representations, respectively. As shown in Fig. 5a, the interaction between the Co and Au atoms is weakened due to a drop in the energy of the d_{z^2} orbital of the Co atom introduced by the change in the symmetry from D_{2d} to D_{4h} (Fig. S34). As $^*\text{OH}$ is adsorbed on Co atom, the adsorbed $^*\text{OH}$ induces a change in the coordinated symmetry of the Au atom from C_{2v} to C_2 owing to the d-orbital symmetry modulating effect of the Co atom (Fig. 5b and Fig. S35). As a result, the

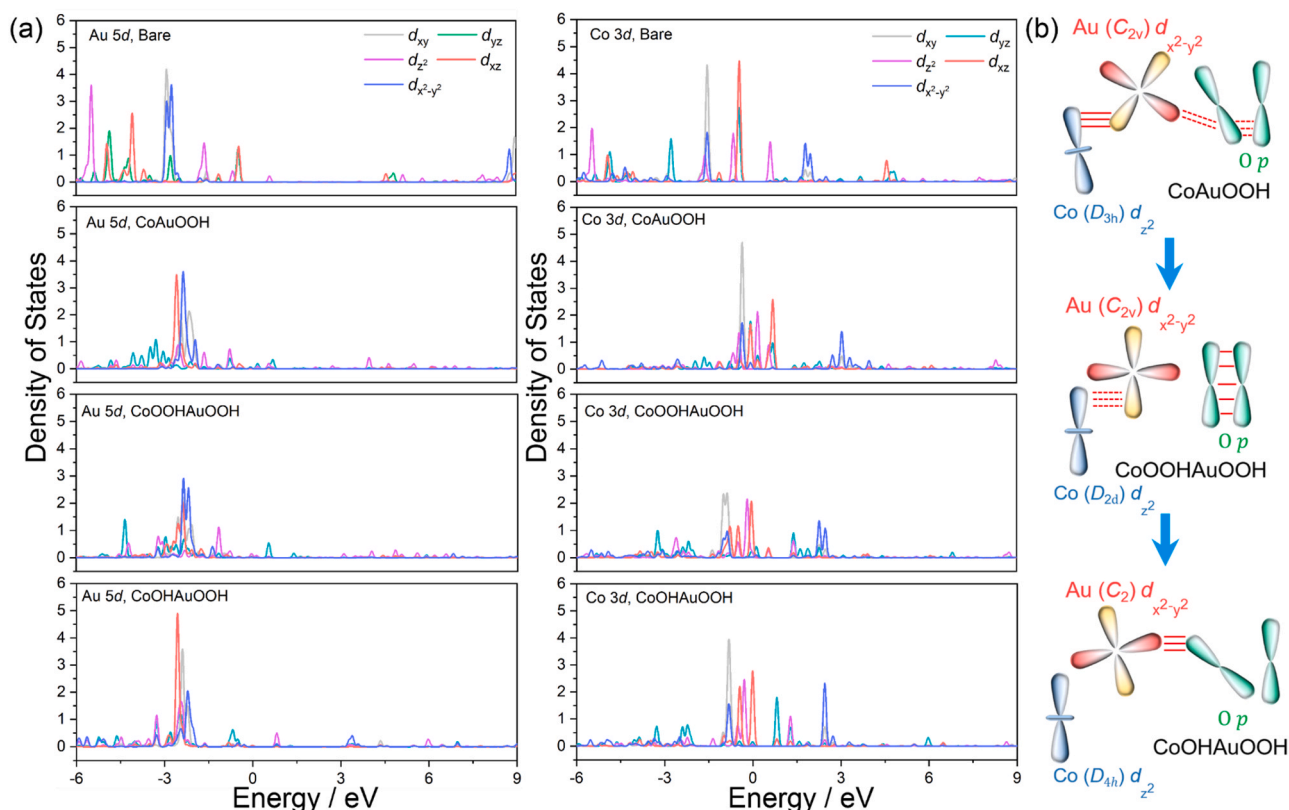


Fig. 5. Electronic structures and the diagram of symmetry modulating mechanism. (a) The PDOS of no intermediates adsorbed (Au-Co) DP-NPAs, $^*\text{OOH}$ adsorbed on Au side, one $^*\text{OOH}$ adsorbed on Co side and one $^*\text{OOH}$ adsorbed on Co side, $^*\text{OH}$ adsorbed on Co side and $^*\text{OOH}$ adsorbed on Au side, respectively. (b) The interaction of $d_{x^2-y^2}$ orbital of Au atom, the d_{z^2} orbital of Co atom and the p orbital of oxygen atoms adsorbed on Au atom dominated by d-orbital symmetry modulating effect of CoAuOOH, CoOOHAuOOH, and CoOHAuOOH, respectively. The dashed line represents the weaker interactions and the real line represent the stronger interactions.

symmetry of the Au atom is improved. As shown in Fig S36, the d_{z^2} orbital of the Co atom scarcely interacts with the $d_{x^2-y^2}$ orbital of the Au atom because of the symmetry change. Consequently, the $d_{x^2-y^2}$ anti-bond spin-orbital declines from a rather high energy level and interacts with *OOH on the oxygen side. Besides, the p_x orbitals of the two oxygen atoms form a non-bonding state with almost no interactions (See in Fig. 5b, S36), thus, boosting the ORR activity. Hence, the d spin-orbital symmetry modulating effect should be considered as the origin of the superior ORR performance.

4. Conclusion

This study describes the design principle and analysis of the heteronuclear (Au–Co) DP-NPAs for an efficient electroreduction of oxygen. The atomically dispersed conjunct (Au–Co) dual-metal sites have been observed via the aberration-corrected HAADF-STEM images. Further, the XAFS analysis verifies that the local structure of the active moieties consists of CoN₂C₂ with the axial Au atom within a porous carbon framework, also supported by the DFT calculations. (Au–Co) DP-NPAs exhibit a significantly improved ORR activity with $E_{1/2}$ of 0.82 V in a harsh acidic electrolyte, along with an enhanced long-term stability with only 15-mV decline in the half-wave potential after long-term stability testing. Besides, (Au–Co) DP-NPAs offers a peak power density of 360 mW cm⁻² in the H₂/air PEM fuel cell system. The manipulated d spin-orbital symmetry has been sufficiently demonstrated to be the main origin of the enhanced ORR performance owing to the modulation of the adsorption and desorption of the adsorbed species. The development of (Au–Co) DP-NPAs via regulation of the d-orbital symmetry represents a highly efficient approach to design the advanced heteronuclear dual atoms with excellent activity, stability and selectivity.

CRediT authorship contribution statement

Jiajun Wang, Xueliang Sun, Geping Yin and Fanpeng Kong: Designing the experiments. **Fanpeng Kong:** Conducting the synthesis and chemical tests. **Fanpeng Kong:** Conducting PEM fuel cell tests. **Junjie Li and Ning Chen:** Performing XAFS tests and fitting data. **Qi Wang and Meng Gu:** Performing the electron microscopy characterization. **Rutong Si and Li-Min Liu:** Conducting First-Principles Calculations. **Jiajun Wang, Xueliang Sun and Fanpeng Kong:** Co-writing the manuscript.

Declaration of Competing Interest

The authors declare that they have no known competing financial interests or personal relationships that could have appeared to influence the work reported in this paper.

Acknowledgements

J. J. Wang thanks the support from “Young Scientists Studio” of Harbin Institute of Technology; X. L. Sun acknowledges the support from Natural Sciences and Engineering Research Council of Canada (NSERC); F. P. Kong thanks the support from China Postdoctoral Science Foundation (No. 2020TQ0084); XAS measurements were conducted at hard X-ray microanalysis (HXMA) beamline at the Canadian Light Source (CLS). Electron microscopy research was performed at Southern University of Science and Technology (Q. Wang and M. Gu); L.M. Liu was supported by the Science Challenge Project (TZ2018004), the Fundamental Research Funds for the Central Universities, the National Natural Science Foundation of China (grant no. 51861130360, 51572016, and U1530401); this research was supported by the Tianhe-2JK computing time award at the Beijing Computational Science Research Center (CSRC) and the high performance computing (HPC) resources at Beihang University.

Appendix A. Supporting information

Supplementary data associated with this article can be found in the online version at doi:10.1016/j.apcatb.2021.120782.

References

- [1] L. Cao, W. Liu, Q. Luo, R. Yin, B. Wang, J. Weissenrieder, M. Soldemo, H. Yan, Y. Lin, Z. Sun, C. Ma, W. Zhang, S. Chen, H. Wang, Q. Guan, T. Yao, S. Wei, J. Yang, J. Lu, Atomically dispersed iron hydroxide anchored on Pt for preferential oxidation of CO in H₂, *Nature* 565 (2019) 631–635.
- [2] J. Li, S. Sharma, K. Wei, Z. Chen, D. Morris, H. Lin, C. Zeng, M. Chi, Z. Yin, M. Muzzio, M. Shen, P. Zhang, A.A. Peterson, S. Sun, Anisotropic strain tuning of L10 ternary nanoparticles for oxygen reduction, *J. Am. Chem. Soc.* 142 (2020) 19209–19216.
- [3] J.E.S. van der Hoeven, J. Jelic, L.A. Olthof, G. Totarella, R.J.A. van Dijk-Moes, J. M. Krafft, C. Louis, F. Studt, A. van Blaaderen, P.E. de Jongh, Unlocking synergy in bimetallic catalysts by core-shell design, *Nat. Mater.* 20 (2021) 1216–1220, <https://doi.org/10.1038/s41563-021-00996-3>.
- [4] Y. Mi, Y. Qiu, Y. Liu, X. Peng, M. Hu, S. Zhao, H. Cao, L. Zhuo, H. Li, J. Ren, X. Liu, J. Luo, Cobalt–iron oxide nanosheets for high-efficiency solar-driven CO₂–H₂O coupling electrocatalytic reactions, *Adv. Funct. Mater.* 30 (2020), 2003438.
- [5] W. Wan, X. Liu, H. Li, X. Peng, D. Xi, J. Luo, 3D carbon framework-supported CoNi nanoparticles as bifunctional oxygen electrocatalyst for rechargeable Zn-air batteries, *Appl. Catal. B: Environ.* 240 (2019) 193–200.
- [6] G.W. Sievers, A.W. Jensen, J. Quinson, A. Zana, F. Bizzotto, M. Oezaslan, A. Dworzak, J.J.K. Kirkensgaard, T.E.L. Smitshuysen, S. Kadkhodazadeh, M. Juelsholt, K.M.O. Jensen, K. Anklam, H. Wan, J. Schafer, K. Cepe, M. Escudero-Escribano, J. Rossmeisl, A. Quade, V. Bruser, M. Arenz, Self-supported Pt-CoO networks combining high specific activity with high surface area for oxygen reduction, *Nat. Mater.* 20 (2021) 208–213.
- [7] X. Shen, T. Nagai, F. Yang, L.Q. Zhou, Y. Pan, L. Yao, D. Wu, Y.S. Liu, J. Feng, J. Guo, H. Jia, Z. Peng, Dual-site cascade oxygen reduction mechanism on SnO x/Pt-Cu-Ni for promoting reaction kinetics, *J. Am. Chem. Soc.* 141 (2019) 9463–9467.
- [8] R. Chattot, O. Le Bacq, V. Beermann, S. Kuhl, J. Herranz, S. Henning, L. Kuhn, T. Asset, L. Guetaz, G. Renou, J. Drnec, P. Bordet, A. Pasturel, A. Eychmuller, T. J. Schmidt, P. Strasser, L. Dubau, F. Maillard, Surface distortion as a unifying concept and descriptor in oxygen reduction reaction electrocatalysis, *Nat. Mater.* 17 (2018) 827–833.
- [9] H. Li, L. Zhang, L. Li, C. Wu, Y. Huo, Y. Chen, X. Liu, X. Ke, J. Luo, G. Van Tendeloo, Two-in-one solution using insect wings to produce graphene-graphite films for efficient electrocatalysis, *Nano Res.* 12 (2019) 33–39.
- [10] R. Qin, K. Liu, Q. Wu, N. Zheng, Surface coordination chemistry of atomically dispersed metal catalysts, *Chem. Rev.* 120 (2020) 11810–11899.
- [11] S. Ott, A. Orfanidi, H. Schmies, B. Anke, H.N. Nong, J. Hübner, U. Gernert, M. Gliche, M. Lerch, P. Strasser, Ionomer distribution control in porous carbon-supported catalyst layers for high-power and low Pt-loaded proton exchange membrane fuel cells, *Nat. Mater.* 19 (2020) 77–85.
- [12] E. Vorobyeva, E. Fako, Z. Chen, S.M. Collins, D. Johnstone, P.A. Midgley, R. Hauert, O.V. Safonova, G. Vile, N. Lopez, S. Mitchell, J. Perez-Ramirez, Atom-by-atom resolution of structure-function relations over low-nuclearity metal catalysts, *Angew. Chem. Int. Ed. Engl.* 58 (2019) 8724–8729.
- [13] B. Qiao, A. Wang, X. Yang, L.F. Allard, Z. Jiang, Y. Cui, J. Liu, J. Li, T. Zhang, Single-atom catalysis of CO oxidation using Pt/FeOx, *Nat. Chem.* 3 (2011) 634–641.
- [14] L. Jiang, K. Liu, S.F. Hung, L. Zhou, R. Qin, Q. Zhang, P. Liu, L. Gu, H.M. Chen, G. Fu, N. Zheng, Facet engineering accelerates spillover hydrogenation on highly diluted metal nanocatalysts, *Nat. Nanotechnol.* 15 (2020) 848–853.
- [15] C. Liu, J. Qian, Y. Ye, H. Zhou, C.-J. Sun, C. Sheehan, Z. Zhang, G. Wan, Y.-S. Liu, J. Guo, S. Li, H. Shin, S. Hwang, T.B. Gunnoe, W.A. Goddard, S. Zhang, Oxygen evolution reaction over catalytic single-site Co in a well-defined brookite TiO₂ nanorod surface, *Nat. Catal.* 4 (2021) 36–45.
- [16] L. Lin, Q. Yu, M. Peng, A. Li, S. Yao, S. Tian, X. Liu, A. Li, Z. Jiang, R. Gao, X. Han, Y.W. Li, X.D. Wen, W. Zhou, D. Ma, Atomically dispersed Ni/α-MoC catalyst for hydrogen production from methanol/water, *J. Am. Chem. Soc.* 143 (2021) 309–317.
- [17] X. Shao, X. Yang, J. Xu, S. Liu, S. Miao, X. Liu, X. Su, H. Duan, Y. Huang, T. Zhang, Iridium Single-atom catalyst performing a quasi-homogeneous hydrogenation transformation of CO₂ to formate, *Chem* 5 (2019) 693–705.
- [18] H. Bao, Y. Qiu, X. Peng, J.-a Wang, Y. Mi, S. Zhao, X. Liu, Y. Liu, R. Cao, L. Zhuo, J. Ren, J. Sun, J. Luo, X. Sun, Isolated copper single sites for high-performance electroreduction of carbon monoxide to multicarbon products, *Nat. Commun.* 12 (2021) 238.
- [19] M. Ouyang, K.G. Papanikolaou, A. Boubnov, A.S. Hoffman, G. Giannakakis, S. R. Bare, M. Stamatakis, M. Flytzani-Stephanopoulos, E.C.H. Sykes, Directing reaction pathways via in situ control of active site geometries in PdAu single-atom alloy catalysts, *Nat. Commun.* 12 (2021) 1549.
- [20] N. Daelman, M. Capdevila-Cortada, N. López, Dynamic charge and oxidation state of Pt/CeO₂ single-atom catalysts, *Nat. Mater.* 18 (2019) 1215–1221.
- [21] Y. Lu, J. Wang, L. Yu, L. Kovarik, X. Zhang, A.S. Hoffman, A. Gallo, S.R. Bare, D. Sokaras, T. Kroll, V. Dagle, H. Xin, A.M. Karim, Identification of the active complex for CO oxidation over single-atom Ir-on-MgAl₂O₄ catalysts, *Nat. Catal.* 2 (2018) 149–156.

- [22] M.T. Greiner, T.E. Jones, S. Beeg, L. Zwiener, M. Scherzer, F. Girgsdies, S. Piccinin, M. Armbruster, A. Knop-Gericke, R. Schlögl, Free-atom-like d states in single-atom alloy catalysts, *Nat. Chem.* 10 (2018) 1008–1015.
- [23] P.N. Duchesne, Z.Y. Li, C.P. Deming, V. Fung, X. Zhao, J. Yuan, T. Regier, A. Aldalbahi, Z. Almarhoon, S. Chen, D.E. Jiang, N. Zheng, P. Zhang, Golden single-atom-site platinum electrocatalysts, *Nat. Mater.* 17 (2018) 1033–1039.
- [24] F. Luo, A. Roy, L. Silviali, D.A. Cullen, A. Zitolo, M.T. Sougrati, I.C. Oğuz, T. Mineva, D. Teschner, S. Wagner, J. Wen, F. Dionigi, U.I. Kramm, J. Rossmeisl, F. Jaouen, P. Strasser, P-block single-metal-site tin/nitrogen-doped carbon fuel cell cathode catalyst for oxygen reduction reaction, *Nat. Mater.* 19 (2020) 1215–1223.
- [25] Y. Nakaya, J. Hirayama, S. Yamazoe, K.-I. Shimizu, S. Furukawa, Single-atom Pt in intermetallics as an ultrastable and selective catalyst for propane dehydrogenation, *Nat. Commun.* 11 (2020) 2838.
- [26] H. Jeong, O. Kwon, B.-S. Kim, J. Bae, S. Shin, H.-E. Kim, J. Kim, H. Lee, Highly durable metal ensemble catalysts with full dispersion for automotive applications beyond single-atom catalysts, *Nat. Catal.* 3 (2020) 368–375.
- [27] L. Lin, S. Yao, R. Gao, X. Liang, Q. Yu, Y. Deng, J. Liu, M. Peng, Z. Jiang, S. Li, Y.-W. Li, X.-D. Wen, W. Zhou, D. Ma, A highly CO-tolerant atomically dispersed Pt catalyst for chemoselective hydrogenation, *Nat. Nanotechnol.* 14 (2019) 354–361.
- [28] D. Li, X. Li, S. Chen, H. Yang, C. Wang, C. Wu, Y.A. Haleem, S. Duan, J. Lu, B. Ge, P. M. Ajayan, Y. Luo, J. Jiang, L. Song, Atomically dispersed platinum supported on curved carbon supports for efficient electrocatalytic hydrogen evolution, *Nat. Energy* 4 (2019) 512–518.
- [29] P. Yin, T. Yao, Y. Wu, L. Zheng, Y. Lin, W. Liu, H. Ju, J. Zhu, X. Hong, Z. Deng, G. Zhou, S. Wei, Y. Li, Single cobalt atoms with precise N-coordination as superior oxygen reduction reaction catalysts, *Angew. Chem. Int. Ed. Engl.* 55 (2016) 10800–10805.
- [30] C. Chen, X. Zhu, X. Wen, Y. Zhou, L. Zhou, H. Li, L. Tao, Q. Li, S. Du, T. Liu, D. Yan, C. Xie, Y. Zou, Y. Wang, R. Chen, J. Huo, Y. Li, J. Cheng, H. Su, X. Zhao, W. Cheng, Q. Liu, H. Lin, J. Luo, J. Chen, M. Dong, K. Cheng, C. Li, S. Wang, Coupling N₂ and CO₂ in H₂O to synthesize urea under ambient conditions, *Nat. Chem.* 12 (2020) 717–724.
- [31] J. Jiao, R. Lin, S. Liu, W.C. Cheong, C. Zhang, Z. Chen, Y. Pan, J. Tang, K. Wu, S. F. Hung, H.M. Chen, L. Zheng, Q. Lu, X. Yang, B. Xu, H. Xiao, J. Li, D. Wang, Q. Peng, C. Chen, Y. Li, Copper atom-pair catalyst anchored on alloy nanowires for selective and efficient electrochemical reduction of CO₂, *Nat. Chem.* 11 (2019) 222–228.
- [32] C.H. Choi, M. Kim, H.C. Kwon, S.J. Cho, S. Yun, H.-T. Kim, K.J.J. Mayrhofer, H. Kim, M. Choi, Tuning selectivity of electrochemical reactions by atomically dispersed platinum catalyst, *Nat. Commun.* 7 (2016) 10922.
- [33] X. Wang, Z. Li, Y. Qu, T. Yuan, W. Wang, Y. Wu, Y. Li, Review of metal catalysts for oxygen reduction reaction: from nanoscale engineering to atomic design, *Chem* 5 (2019) 1486–1511.
- [34] H. Fei, J. Dong, Y. Feng, C.S. Allen, C. Wan, B. Voloskiy, M. Li, Z. Zhao, Y. Wang, H. Sun, P. An, W. Chen, Z. Guo, C. Lee, D. Chen, I. Shakir, M. Liu, T. Hu, Y. Li, A. I. Kirkland, X. Duan, Y. Huang, General synthesis and definitive structural identification of MN₄C₄ single-atom catalysts with tunable electrocatalytic activities, *Nat. Catal.* 1 (2018) 63–72.
- [35] J. Wang, Z. Huang, W. Liu, C. Chang, H. Tang, Z. Li, W. Chen, C. Jia, T. Yao, S. Wei, Y. Wu, Y. Li, Design of N-coordinated dual-metal sites: a stable and active Pt-free catalyst for acidic oxygen reduction reaction, *J. Am. Chem. Soc.* 139 (2017) 17281–17284.
- [36] W. Ren, X. Tan, W. Yang, C. Jia, S. Xu, K. Wang, S.C. Smith, C. Zhao, Isolated diatomic Ni-Fe metal-nitrogen sites for synergistic electroreduction of CO₂, *Angew. Chem. Int. Ed. Engl.* 58 (2019) 6972–6976.
- [37] J. Xu, S. Lai, D. Qi, M. Hu, X. Peng, Y. Liu, W. Liu, G. Hu, H. Xu, F. Li, C. Li, J. He, L. Zhu, J. Sun, Y. Qiu, S. Zhang, J. Luo, X. Liu, Atomic Fe-Zn dual-metal sites for high-efficiency pH-universal oxygen reduction catalysis, *Nano Res.* 14 (2021) 1374–1381.
- [38] M. Mon, M.A. Rivero-Crespo, J. Ferrando-Soria, A. Vidal-Moya, M. Boronat, A. Leyva-Perez, A. Corma, J.C. Hernandez-Garrido, M. Lopez-Haro, J.J. Calvino, G. Ragazzon, A. Credi, D. Armentano, E. Pardo, Synthesis of densely packaged, ultrasmall PtO₂ clusters within a thioether-functionalized MOF: catalytic activity in industrial reactions at low temperature, *Angew. Chem. Int. Ed. Engl.* 57 (2018) 6186–6191.
- [39] S. Tian, B. Wang, W. Gong, Z. He, Q. Xu, W. Chen, Q. Zhang, Y. Zhu, J. Yang, Q. Fu, C. Chen, Y. Bu, L. Gu, X. Sun, H. Zhao, D. Wang, Y. Li, Dual-atom Pt heterogeneous catalyst with excellent catalytic performances for the selective hydrogenation and epoxidation, *Nat. Commun.* 12 (2021) 3181.
- [40] X. Han, X. Ling, D. Yu, D. Xie, L. Li, S. Peng, C. Zhong, N. Zhao, Y. Deng, W. Hu, Atomically dispersed binary Co-Ni sites in nitrogen-doped hollow carbon nanocubes for reversible oxygen reduction and evolution, *Adv. Mater.* 31 (2019) 1905622.
- [41] A. Han, X. Wang, K. Tang, Z. Zhang, C. Ye, K. Kong, H. Hu, L. Zheng, P. Jiang, C. Zhao, Q. Zhang, D. Wang, Y. Li, An adjacent atomic platinum site enables single-atom iron with high oxygen reduction reaction performance, *Angew. Chem. Int. Ed. Engl.* 60 (2021) 19262–19271.
- [42] R. Gao, J. Wang, Z.-F. Huang, R. Zhang, W. Wang, L. Pan, J. Zhang, W. Zhu, X. Zhang, C. Shi, J. Lim, J.-J. Zou, *Nat. Energy* (2021), <https://doi.org/10.1038/s41560-021-00826-5>.
- [43] G. Yang, J. Zhu, P. Yuan, Y. Hu, G. Qu, B.A. Lu, X. Xue, H. Yin, W. Cheng, J. Cheng, W. Xu, J. Li, J. Hu, S. Mu, J.N. Zhang, Regulating Fe-spin state by atomically dispersed Mn-N in Fe-N-C catalysts with high oxygen reduction activity, *Nat. Commun.* 12 (2021) 1734.
- [44] H. Yan, Y. Lin, H. Wu, W. Zhang, Z. Sun, H. Cheng, W. Liu, C. Wang, J. Li, X. Huang, T. Yao, J. Yang, S. Wei, J. Lu, Bottom-up precise synthesis of stable platinum dimers on graphene, *Nat. Commun.* 8 (2017) 1070.
- [45] M. Xiao, Y. Chen, J. Zhu, H. Zhang, X. Zhao, L. Gao, X. Wang, J. Zhao, J. Ge, Z. Jiang, S. Chen, C. Liu, W. Xing, Climbing the apex of the ORR volcano plot via binuclear site construction: electronic and geometric engineering, *J. Am. Chem. Soc.* 141 (2019) 17763–17770.
- [46] J. Wang, W. Liu, G. Luo, Z. Li, C. Zhao, H. Zhang, M. Zhu, Q. Xu, X. Wang, C. Zhao, Y. Qu, Z. Yang, T. Yao, Y. Li, Y. Lin, Y. Wu, Y. Li, Synergistic effect of well-defined dual sites boosting the oxygen reduction reaction, *Energy Environ. Sci.* 11 (2018) 3375–3379.
- [47] M. Xiao, H. Zhang, Y. Chen, J. Zhu, L. Gao, Z. Jin, J. Ge, Z. Jiang, S. Chen, C. Liu, W. Xing, Identification of binuclear Co₂N₅ active sites for oxygen reduction reaction with more than one magnitude higher activity than single atom CoN₄ site, *Nano Energy* 46 (2018) 396–403.
- [48] Z. Lu, B. Wang, Y. Hu, W. Liu, Y. Zhao, R. Yang, Z. Li, J. Luo, B. Chi, Z. Jiang, M. Li, S. Mu, S. Liao, J. Zhang, X. Sun, An isolated zinc-cobalt atomic pair for highly active and durable oxygen reduction, *Angew. Chem. Int. Ed. Engl.* 58 (2019) 2622–2626.
- [49] S. Zhao, Y. Wang, J. Dong, C.-T. He, H. Yin, P. An, K. Zhao, X. Zhang, C. Gao, L. Zhang, J. Lv, J. Wang, J. Zhang, A.M. Khattak, N.A. Khan, Z. Wei, J. Zhang, S. Li, H. Zhao, Z. Tang, Ultrathin metal-organic framework nanosheets for electrocatalytic oxygen evolution, *Nat. Energy* 1 (2016) 16184.
- [50] Y. Chen, R. Gao, S. Ji, H. Li, K. Tang, P. Jiang, H. Hu, Z. Zhang, H. Hao, Q. Qu, X. Liang, W. Chen, J. Dong, D. Wang, Y. Li, Atomic-level modulation of electronic density at cobalt single-atom sites derived from metal-organic frameworks: enhanced oxygen reduction performance, *Angew. Chem. Int. Ed.* 60 (2021) 3212–3221.
- [51] M. Melchionna, P. Fornasiero, High Pt single-atom density for high-rate generation of H₂O₂, *Chem* 5 (2019) 1927–1928.
- [52] L. Lin, W. Zhou, R. Gao, S. Yao, X. Zhang, W. Xu, S. Zheng, Z. Jiang, Q. Yu, Y.W. Li, C. Shi, X.D. Wen, D. Ma, Low-temperature hydrogen production from water and methanol using Pt/ α -MoC catalysts, *Nature* 544 (2017) 80–83.
- [53] H. Li, L. Wang, Y. Dai, Z. Pu, Z. Lao, Y. Chen, M. Wang, X. Zheng, J. Zhu, W. Zhang, R. Si, C. Ma, J. Zeng, Synergetic interaction between neighbouring platinum monomers in CO₂ hydrogenation, *Nat. Nanotechnol.* 13 (2018) 411–417.
- [54] T.N. Ye, Z. Xiao, J. Li, Y. Gong, H. Abe, Y. Niwa, M. Sasase, M. Kitano, H. Hosono, Stable single platinum atoms trapped in sub-nanometer cavities in 12CaO-7Al₂O₃ for chemoselective hydrogenation of nitroarenes, *Nat. Commun.* 11 (2020) 1020.
- [55] T.D. Kuehne, M. Iannuzzi, M. Del Ben, V.V. Rybkin, P. Seewald, F. Stein, T. Laino, R.Z. Khalullin, O. Schutt, F. Schiffrmann, D. Golze, J. Wilhelm, S. Chulkov, M. H. Bani-Hashemian, V. Weber, U. Borstnik, M. Tallefiumier, A.S. Jakobovits, A. Lazzaro, H. Pabst, T. Mueller, R. Schade, M. Guidon, S. Andermatt, N. Holmberg, G.K. Schenter, A. Hehn, A. Bussy, F. Belleflamme, G. Tabacchi, A. Gloss, M. Lass, I. Bethune, C.J. Mundy, C. Plessl, M. Watkins, J. VandeVondele, M. Krack, J. Hutter, CP2K: an electronic structure and molecular dynamics software package - quickstep: efficient and accurate electronic structure calculations, *J. Chem. Phys.* 152 (2020), 194103.
- [56] J.M. Tao, J.P. Perdew, V.N. Staroverov, G.E. Scuseria, Climbing the density functional ladder: nonempirical meta-generalized gradient approximation designed for molecules and solids, *Phys. Rev. Lett.* 91 (2003), 146401.
- [57] C. Hartwigsen, S. Goedecker, J. Hutter, Relativistic separable dual-space Gaussian pseudopotentials from H to Rn, *Phys. Rev. B* 58 (1998) 3641–3662.
- [58] J. VandeVondele, J. Hutter, Gaussian basis sets for accurate calculations on molecular systems in gas and condensed phases, *J. Chem. Phys.* 127 (2007), 114105.
- [59] O. Andreussi, I. Dabo, N. Marzari, Revised self-consistent continuum solvation in electronic-structure calculations, *J. Chem. Phys.* 136 (2012), 064102.
- [60] X. Xie, C. He, B. Li, Y. He, D.A. Cullen, E.C. Wegener, A.J. Kropf, U. Martinez, Y. Cheng, M.H. Engelhard, M.E. Bowden, M. Song, T. Lemmon, X.S. Li, Z. Nie, J. Liu, D.J. Myers, P. Zelenay, G. Wang, G. Wu, Y. Ramani, Y. Shao, Performance enhancement and degradation mechanism identification of a single-atom Co–N–C catalyst for proton exchange membrane fuel cells, *Nat. Catal.* 3 (2020) 1044–1054.
- [61] X.X. Wang, D.A. Cullen, Y.T. Pan, S. Hwang, M. Wang, Z. Feng, J. Wang, M. H. Engelhard, H. Zhang, Y. He, Y. Shao, D. Su, K.L. More, J.S. Spendlow, G. Wu, Nitrogen-coordinated single cobalt atom catalysts for oxygen reduction in proton exchange membrane fuel cells, *Adv. Mater.* 30 (2018), 1706758.
- [62] T. Sun, S. Zhao, W. Chen, D. Zhai, J. Dong, Y. Wang, S. Zhang, A. Han, L. Gu, R. Yu, X. Wen, H. Ren, L. Xu, C. Chen, Q. Peng, D. Wang, Y. Li, *Proc. Natl. Acad. Sci. U. S. A.* 115 (2018) 12692–12697.
- [63] Y. Han, Y.-G. Wang, W. Chen, R. Xu, L. Zheng, J. Zhang, J. Luo, R.A. Shen, Y. Zhu, W.C. Cheong, C. Chen, Q. Peng, D. Wang, Y. Li, Hollow N-doped carbon spheres with isolated cobalt single atomic sites: superior electrocatalysts for oxygen reduction, *J. Am. Chem. Soc.* 139 (2017) 17269–17272.
- [64] J. Zhang, J. Liu, L. Xi, Y. Yu, N. Chen, S. Sun, W. Wang, K.M. Lange, B. Zhang, Single-atom Au/NiFe layered double hydroxide electrocatalyst: probing the origin of activity for oxygen evolution reaction, *J. Am. Chem. Soc.* 140 (2018) 3876–3879.
- [65] L. Zhang, R. Si, H. Liu, N. Chen, Q. Wang, K. Adair, Z. Wang, J. Chen, Z. Song, J. Li, M.N. Banis, R. Li, T.-K. Sham, M. Gu, L.-M. Liu, G.A. Botton, X. Sun, Atomic layer deposited Pt-Ru dual-metal dimers and identifying their active sites for hydrogen evolution reaction, *Nat. Commun.* 10 (2019) 4936.
- [66] L. Zhang, Q. Wang, R. Si, Z. Song, X. Lin, M.N. Banis, K. Adair, J. Li, K. Doyle-Davis, R. Li, L.-M. Liu, M. Gu, X. Sun, New insight of pyrrole-like nitrogen for boosting hydrogen evolution activity and stability of Pt single atoms, *Small* 17 (2021), 2004453.